ROYAL SOCIETY OF CHEMISTRY

PAPER

CrossMark
click for updates

Nanoporous networks as caging supports for uniform, surfactant-free Co_3O_4 nanocrystals and their applications in energy storage and conversion†

Jeehye Byun,[a] Hasmukh A. Patel,[a] Dong Jun Kim,[b] Chan Ho Jung,[ac]
Jeong Young Park,*[ac] Jang Wook Choi*[a] and Cafer T. Yavuz*[a]

We report a new, surfactant-free method to produce Co_3O_4 nanocrystals with controlled sizes and high dispersity by caging templation of nanoporous networks. The morphologies of Co_3O_4 nanoparticles differ from wires to particulates by simply varying solvents. The composites of nanoparticles within network polymers are highly porous and are promising for many applications where accessible surface and aggregation prevention are important. The electrochemical performance of the composites demonstrates superior capacity and cyclic stability at a high current density (~980 mA h g^{-1} at the 60th cycle at a current density of 1000 mA g^{-1}). In a catalytic oxidation reaction of carbon monoxide, the composites exhibit a remarkable stability (in excess of 35 hours) and catalytic performance ($T_{100} = 100$ °C).

Introduction

Great interest in nanomaterials is mainly due to the fact that the properties of materials can be adjusted with their size and shape.[1] The optical, thermal, and electrical properties of nanomaterials vary with their size distribution and morphologies, therefore the ability to tune the structure, size and shape of nanomaterials has utmost importance in nanotechnology. Nanomaterials with controlled morphology and structure lead to key developments in many application areas such as solar cells,[2,3] heterogeneous catalysts,[4–6] water treatment adsorbents,[7] and Li-ion battery electrodes.[8] Surfactants are often used in manufacturing stable dispersions of individual nanoparticulates.[7] When nanocrystals are needed to be immobilized, self-assembly techniques are chosen[9,10] despite the lack of precise control in packing density and continuity. In order to control the morphology of the nanomaterials on a wider scale, template-assisted synthesis is most commonly used since this approach could produce highly ordered structures with tailorable supports. Hard templates such as mesoporous silicas (*i.e.*, KIT-16, SBA-15, MCM-41 and MOFs)[11–15] and soft templates such

as biomolecules and block copolymers[16,17] have been utilized to generate nanomaterials with uniform structures. Hard templates can produce well-organized structures with good pore regularity and crystallinity; however, the structures largely depend on manipulation of preparation conditions. Soft templates, with large structural variation, have an advantage since the templates not only bear nanoparticles *via* a facile supramolecular interaction with inorganic precursors, but also they could improve structural stability and surface properties owing to their molecular rigidity and functionalities. In any proposed preparation scheme, it is desired that nanocrystals show their full potential by keeping their surface unobstructed by either surfactants or solid substrates.

Porous network polymers with nanoscale porosity (pore sizes under 100 nm), *e.g.* covalent organic polymers (COPs), have attracted significant attention due to their potential in a wide variety of applications such as gas storage, heterogeneous catalysis, contaminant adsorption, and electric devices.[18–25] The main advantages of COPs are designable pore structures and synthetic diversity with various building blocks for target applications.[26] Recently, Zhou *et al.* reported that COPs with a high surface area are utilized as a soft template to generate Pd nanoparticles. The Pd nanoparticles, impregnated into COPs with *in situ* reduction, are highly uniform, and the composites made out of COPs and Pd particles exhibit excellent performance as a heterogeneous catalyst for CO oxidation.[27] Despite the high activity, they employed glow discharge to improve the dispersity to reduce the size of nanoparticles, leading to degradation in the original binding ability of COPs. Impregnation also reduced the surface areas considerably, hindering

[a]Graduate School of EEWS, Korea Advanced Institute of Science and Technology (KAIST), Daejeon 305-701, Republic of Korea. E-mail: yavuz@kaist.ac.kr; jangwookchoi@kaist.ac.kr

[b]Department of Materials Science and Engineering, Korea Advanced Institute of Science and Technology (KAIST), Daejeon 305-701, Republic of Korea

[c]Center for Nanomaterials and Chemical Reactions, Institute for Basic Science, Daejeon 305-701, Republic of Korea. E-mail: jeongypark@kaist.ac.kr

effective diffusion of gas molecules. The complete conversion temperatures of CO (T_{100}) were found to be 185–200 °C, even though a highly active catalyst, palladium, was used.

Herein, we introduce newly designed COPs to produce cobalt oxide nanocrystals with controlled sizes and high dispersity. The cobalt ions were bound onto the porous polymer with amide functionalities and simply converted into oxide nanoparticles with a base treatment and annealing. The morphology of nanoparticles was controlled from wires to particulates by simply varying solvents, due to different wettabilities of polymers. We believe that the proposed synthetic approach could offer a new surfactant-free method to produce uniform oxide nanoparticles with a rigid polymeric support. The caged, rattling nanocrystals with unoccupied surface exhibit expected electrochemical properties and catalytic reactivities for energy storage and conversion. We, therefore, used nanocomposites as active materials for an anode in lithium ion batteries and a heterogeneous catalyst in CO oxidation reactions.

Experimental

Synthesis of COPs

In a typical synthesis, DIPEA (N,N-diisopropylethylamine, 6.55 mL, 37.6 mmol) was added to 1,4-phenylene diamine (1.65 g, 15.23 mmol) dissolved in 1,4-dioxane (250 mL) at room temperature. The 1,4-dioxane solution (50 mL) with 1,3,5-benzene tricarbonyltrichloride (2.5 g, 9.42 mmol) was added dropwise to the above solution with continuous stirring at room temperature under atmospheric conditions. The mixture was aged for 24 h, and the whitish precipitate was washed with 1,4-dioxane and soaked in ethyl alcohol three times over a period of 12 h. The obtained product (coded as COP-33 and henceforth used as just "COP") was dried at room temperature under vacuum for 2 h. Yield: 86%. The synthesis was repeated at least three times with quantities exceeding 1 gram, to prove reproducibility.

Synthesis of Co_3O_4 nanoparticles incorporated into COPs

In a typical synthesis, COP powder (0.1 g) was dispersed into the desired solvent (20 mL, either EtOH and DMF 1 : 1 v/v mixture or water) and the aqueous solution of cobalt nitrate hexahydrate (0.2 M, 10 mL) was added at once. The mixture was tumbled for 24 h on an end-over-end rotator (8 rpm) for the dispersion of cobalt ions inside of COPs. The mixture was then subjected to gravitational sedimentation (8000 rpm) and two-thirds of supernatant solution was decanted. Aqueous sodium hydroxide solution (0.15 M, 20 mL) was added into the mixture and was further aged for 6 h with constant tumbling. Finally, the powder was filtered and washed with DI water and ethyl alcohol several times. The obtained product was dried at room temperature and annealed at 300 °C for 1 h in air.

Characterisation

XRD (X-ray Diffraction) patterns of the samples were acquired from 10 to 80° by using a Rigaku D/MAX-2500 Multi-purpose High Power X-ray diffractometer. XPS (X-ray Photoelectron Spectroscopy) spectra were obtained using a Thermo VG Scientific Sigma Probe system equipped with an Al-Kα X-ray source (1486.3 eV) with an energy resolution of 0.47 eV FWHM under UHV conditions of 10^{-10} Torr. FTIR spectra were obtained on KBr pellets using a Perkin-Elmer FT-IR spectrometer equipped with a diffuse reflectance accessory. The IR and DRIFT spectra were recorded at a resolution of 4 cm^{-1} and 64 scans. FE-TEM (Field Emission Transmission Electron Microscopy) was conducted by using a Tecnai G2 F30, 300 kV. FE-SEM (Field Emission Scanning Electron Microscopy) was performed using a Nova 230. In order to find out the porosity of powder samples, nitrogen adsorption isotherms were obtained with a Micromeritics ASAP 2020 accelerated surface area and porosimetry analyzer at 77 K after the samples were degassed at 150 °C for 5 h under vacuum. The surface area of the samples was evaluated by the Brunauer–Emmett–Teller (BET) method. The quantitative analysis of the loaded metal concentration was measured by ICP-MS (Inductively Coupled Plasma Mass Spectroscopy, Agilent 7700 s). The samples for ICP-MS were acidified with nitric acid and subsequently diluted with deionized water. TGA (Thermogravimetric analysis) was performed on a NETZSCH-TG 209 F3 instrument by heating the samples up to 800 °C at 10 °C min^{-1} in an N$_2$ and air atmosphere.

Electrochemical measurements

All of electrochemical measurements were performed via a WBCS 3000 battery cycler (Wonatech, Korea), using coin type cells assembled in an argon-filled glovebox. The working electrodes were prepared by making slurry with 60 wt% active material, 30 wt% carbon black and 10 wt% polyvinylidene fluoride (PVdF) dissolved in N-methyl-2-pyrrolidinone (NMP). After coating the above slurries on Cu foils, the electrodes were dried at 70 °C in a vacuum overnight in order to remove the solvent. The mass loading of the active material on the electrode was about 0.5 mg cm^{-2}. The metallic lithium foil (Hosen, Japan) was used as the reference electrode and counter electrode. A Celgard 2302 membrane was used as a separator and 1 M of lithium hexafluorophosphate (LiPF$_6$) dissolved in a mixture of ethylene carbonate and diethyl carbonate (1 : 1 v/v) was used as an electrolyte. The galvanostatic charge/discharge cycles were performed at various current densities of 50–2000 mA g^{-1} between 0.05 and 3.0 V vs Li/Li$^+$ at 25 °C. The specific capacity was calculated based upon the amount of Co$_3$O$_4$ loaded on the COP structure, which was derived from ICP-MS analysis.

Catalytic reaction measurements

CO oxidation was performed with nanocomposites in a flow reactor that was described elsewhere.[28] About 100 mg of the composites was loaded into a quartz tube, and the powder was reduced at 250 °C under H$_2$ flow with He balance gas (5% H$_2$ in He, a flow of 45 mL min^{-1}) for 30 min to remove hydrocarbon contaminants on the catalyst. The catalyst was cooled down to room temperature, and subsequently reacted under the gas mixture with the composition of 4% CO, 10% O$_2$, and 86% He (balance). The total gas flow rate was controlled to be 50 mL min^{-1} with a mass flow controller (Brooks Instrument). CO

15490 | *J. Mater. Chem. A*, 2015, **3**, 15489–15497

This journal is © The Royal Society of Chemistry 2015

oxidation was carried out until CO was converted 100% into CO_2 in the temperature range of 25–120 °C. There was no CO conversion observed in the empty reactor, and the gas mixture passing through the quartz tube was monitored by using gas chromatography (GC, DS Science).

Results and discussion

Morphology and chemical composition of Co_3O_4–COP composites

A representative TEM image shows the morphology of Co_3O_4 nanoparticles impregnated into COP structures. Fig. 1a displays the composites with near spherical nanoparticles and Fig. 1b exhibits needle-like nanowires. The nanoparticles and nanowires were produced in different solvent systems; solvent mixture (ethanol and DMF 1 : 1 v/v) and water, respectively. The nanocomposites with nanoparticles are denoted as npCOP (np = nanoparticle), and the composites with nanowires are named as nwCOP (nw = nanowire) for convenience. The particles were found to be incorporated into the COP, and the size of the particles was nearly uniform. For npCOP, the average diameter of the particles is 10.82 ± 1.88 nm; for nwCOP, the length of the particles is 38.36 ± 12.7 nm and the width is 3.036 ± 0.816 nm. Even at low magnifications of TEM images, the size distributions of npCOP and nwCOP are found to be highly uniform, which is unusual in synthesis without a surfactant (Fig. S1†). The HRTEM image reveals that npCOP (Fig. 1c) and nwCOP (Fig. 1d) exhibit single crystalline structures, clearly displaying lattice fringes with $d = 0.467$ nm, which is attributed to the (111) plane of spinel Co_3O_4. Fig. 1e displays a SEM image of a bare COP with tadpole-like morphology. The uniform structure of Co_3O_4 nanoparticles is believed to result from the caging effect of COPs with an organized pore structure.[29] In order to verify the templation by COPs, Co_3O_4 nanoparticles were synthesized within several amide-based porous polymers instead of utilizing COPs. The structures with 2,3,5,6-tetramethyl-1,4-phenylenediamine (COP-58, Fig. S2a†) and 2,5-dimethyl-1,4-phenylenediamine (COP-59, Fig. S2b†) linkers, which are similar to phenylenediamine linkers of COPs, produced needle-like nanoparticles in several places under the same experimental conditions with nwCOP. However, due to the steric hindrance of methyl groups, the morphology of nanoparticles is not as much uniform as the one of nwCOP. The other structures with 4,4'-oxydianiline (COP-43, Fig. S2c†) and 1,5-diaminonaphthalein (COP-45, Fig. S2d†) linkers did not generate uniform nanoparticles. We confirmed that COPs with phenylenediamine linkers only produced uniform Co_3O_4 nanoparticles in aqueous solution. Similarly, when bare Co_3O_4 nanoparticles were generated with the same procedure of npCOP and nwCOP in the absence of COPs, the morphology of nanoparticles was irregular and particles were mostly aggregated (Fig. 1f and g).

The XRD patterns of npCOP and nwCOP (Fig. 2a) reveal that the peaks of Co_3O_4 spinel (JCPDS # 00-043-1003, fcc, $Fd3m$ (227), $a = 0.808$ nm) were formed. The diffraction peaks at a 2θ value correspond to diffraction planes of (111), (220), (311), (222), (400), (422), (511), (440) and (533), showing the presence of homogeneous Co_3O_4. The chemical composition of
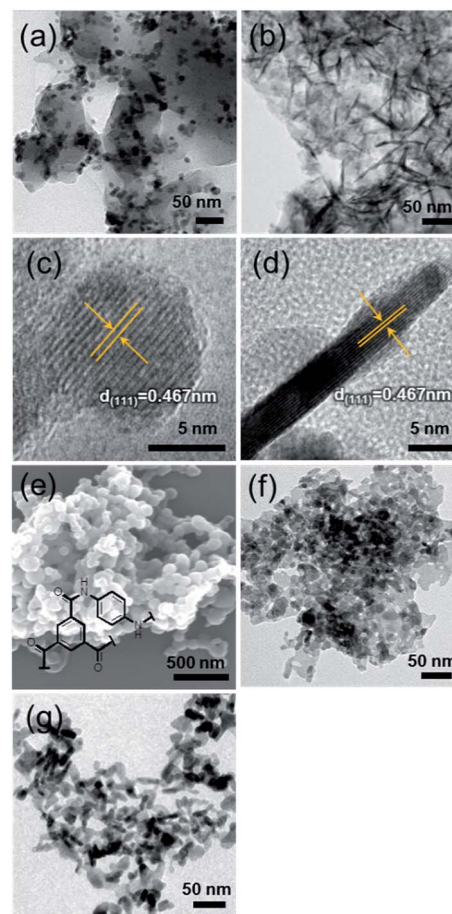

Fig. 1 TEM morphology of (a) npCOP and (b) nwCOP. High resolution TEM of (c) npCOP and (d) nwCOP with the lattice spacing measurement. (e) SEM image of bare COP displaying with its chemical structure. Bare Co_3O_4 nanoparticles synthesized without COP templates (f) in the EtOH/DMF mixture and (g) in water.

nanocomposites was determined by XPS measurements in the region of 1–1300 eV (Fig. S3a†). The Co 2p XPS spectrum of the nanocomposites displays two distinctive peaks at around 795 and 779.8 eV, corresponding to Co $2p_{1/2}$ and Co $2p_{3/2}$ spin–orbit peaks of Co_3O_4 (Fig. S3b†).[30] Fig. 2b displays FTIR spectra of bare COP and their composites with Co_3O_4 nanoparticles. The IR spectrum of COPs demonstrated the existence of secondary amide functionality with the stretching vibrations at about 3380 cm^{-1} (N–H) and 1650 cm^{-1} (C=O). The absorption peaks around 1520 cm^{-1} and 1400 cm^{-1} correspond to C–N–H and C–N stretching vibration, respectively. The peaks around 1290 cm^{-1} can be assigned to C=C from aromatic rings, whereas the absorption band at 1216 cm^{-1} is due to the aromatic C–H in-plane bending mode, and the out-of-plane deformations of C–H in the 1,3,5-substituted benzene ring result in a band at about 830 cm^{-1}. The IR spectrum of the npCOP composites is mostly identical to the one of COPs, however, the spectrum of the nwCOP composites shows the change of the stretching vibrations in the amide region. The change of spectrum results from the strong interaction between nanowires and amide functional groups. It seems that the linkage between trimesoyl and amine

were weakened due to the formation of the highly intrusive large nanowires, so that the IR spectrum of the secondary amide was shifted. The original peak near at 3380 cm^{-1}, which can be assigned to the secondary amide, was split into 3590 cm^{-1} and 3150 cm^{-1} in the case of nwCOP, perhaps due to the strong interaction of cobalt ions with the amide functionalities. The peak at 1615 cm^{-1} (the point marked with an asterisk), which corresponds to the N–H bond of the amine that is adjacent to a carbonyl, also became stronger. Two distinct bands at around 560 cm^{-1} and 670 cm^{-1} appeared in both npCOP and nwCOP composites (Fig. S4† for a magnification). The band at 560 cm^{-1} is associated with the OM_3 vibration in the spinel structure, where M indicates Co^{3+} in an octahedral hole. The band at 670 cm^{-1} is attributed to the $M'MO_3$ vibration, where M' is from the Co^{2+} in a tetrahedral hole. These bands confirm that the Co_3O_4 spinel phase is formed in both the composites.

The uniform structures of nanoparticles indicate that COPs have a unique and organized pore structure unlike other amorphous porous carbons.[29] The control in the morphology of nanoparticles is, therefore, achieved by different solvent systems (Scheme 1). This may be attributed to the different wetting properties of COPs in different solvents.[27] Since the organic solvents have higher affinity with COP structures, the solvent with the mixture of ethanol and DMF can easily penetrate through the inside of COPs, so that cobalt metals can be deeply injected into the structures. The embedded metals are grown under nanoscale confinement induced from pore structures,[31] therefore the size of nanoparticles synthesized in the organic solvent could be reduced. On the other hand, water has less affinity with COP structure and the cobalt metals are closely attached to the larger pores of the COP. Therefore, the composites produced in the solvent mixture have highly dispersed nanoparticles with small sizes, while the composites produced in water exhibit larger particles with wire shapes which results from the mesopore templation. This phenomenon also corresponds to the degree of dispersion of Co_3O_4 nanoparticles. Backscattered electron SEM images (Scheme 1c and d) exhibit that the nanoparticles in npCOP are well distributed on COPs while the nanowires are aggregated on the periphery of COPs. The npCOP could get soaked in the organic solvent, so that cobalt ions are dispersed throughout the COP structure, resulting in homogeneous distribution of Co_3O_4 nanoparticles. However, in the case of nwCOP, the cobalt ions are not able to penetrate COPs in water, finally leading to form aggregates on the surface of COPs.

Table 1 displays the particle loading percentage and pore distribution of npCOP and nwCOP. The amount of Co_3O_4 loaded on the COP was calculated based upon the cobalt concentration measured from ICP-MS. The loading percentage of npCOP was much higher than that of nwCOP, and this implies that the adsorbed amount of metals is larger in the solvent mixture since the dispersion of metals was much easier in the organic solvent system with a deep penetration. Besides, the pore structure of npCOP and nwCOP also differs from each other due to the solvent effect. The initial surface area of bare
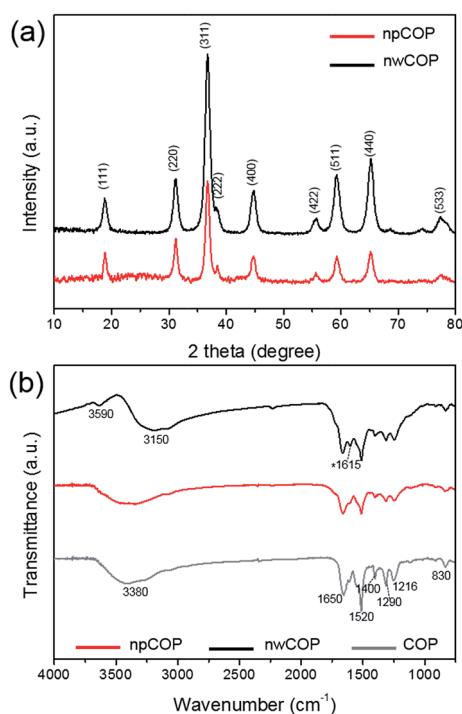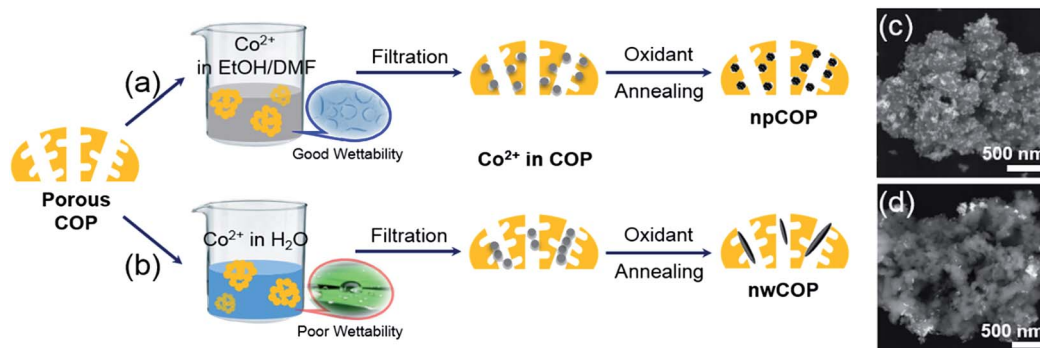

Fig. 2 (a) X-ray diffraction patterns of npCOP and nwCOP, and (b) FTIR spectra obtained from the composites and bare COP itself.

Scheme 1 Schematic illustration of the *in situ* nanocrystal growth mechanism resulted from different wettability of COPs in (a) organic solvent mixture (ethanol and DMF) and (b) water. BSE-SEM images of (c) npCOP and (d) nwCOP.

15492 | *J. Mater. Chem. A*, 2015, **3**, 15489–15497

This journal is © The Royal Society of Chemistry 2015

COPs was 53.2 m^2 g^{-1}, however, the surface area of npCOP and nwCOP increased up to 2.9 and 2.5 times, respectively. Since small nanoparticles are distributed throughout COP structures, the surface area of the composites increases. The increase in the surface area is expected as pores are being filled with new surface bearing particles. This also agrees with a rattle-like composition rather than a tight fit. The decrease of pore volume in npCOP is attributed to the impregnation of small nanoparticles into the inner structure. On the other hand, in the case of nwCOP, the highly anisotropic nanowires are attached and packed in mesopores with close disposition to the surface of the COP, so that rooms between wires may contribute to the increase of pore volume without compromising the pore space of COP itself. As expected, pore diameters of both npCOP and nwCOP were smaller than that of original COP, and the pore size of npCOP is much decreased compared to the width of nwCOP owing to the inner packing of nanoparticles.

Table 1 Loading percentage and pore distribution of bare COP and the nanocomposites, where SA$_{BET}$: BET surface area; V_p: total pore volume; and d_p: BJH adsorption average pore diameter

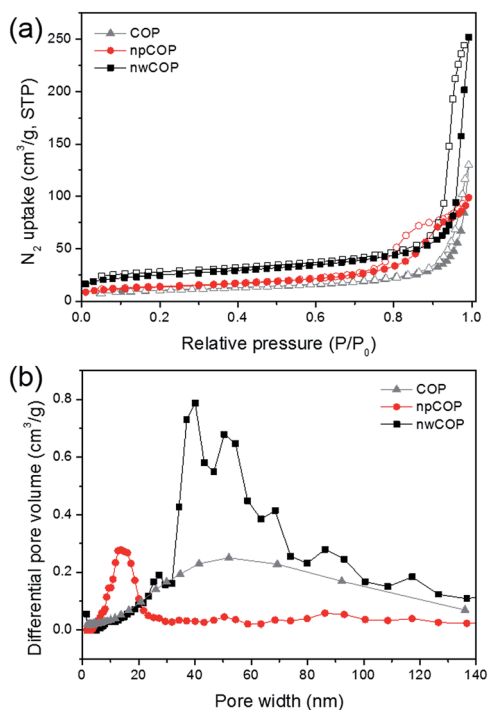|	npCOP	nwCOP	COP
Co$_3$O$_4$ loading (%)	80.12	67.7	—
SA$_{BET}$ (m^2 g^{-1})	154.55	133.7	53.2
V_p (cm^3 g^{-1})	0.153	0.39	0.2
d_p (nm)	12.67	17.62	21.49

Fig. 3 (a) N$_2$ adsorption–desorption isotherm of npCOP, nwCOP and bare COP measured at 77 K, and (b) pore size *versus* differential pore volume of the bare COP and the nanocomposites.

Fig. 3a shows N$_2$ adsorption isotherms and pore distribution of the nanocomposites. Bare COP and nwCOP exhibit a *type II* isotherm reversible sorption isotherm, indicating that an indefinite multi-layer was formed after the monolayered adsorption was completed (flat range). This isotherm is found in materials with a wide distribution of pore sizes, and Fig. 3b confirms that nwCOP has a broad pore distribution. In the case of npCOP, it displays a *type IV* isotherm, which is a variation of *type II* isotherm, with a finite multilayer formation due to complete packing of pores. This corresponds to a narrow pore distribution of npCOP (Fig. 3b), compared to that of COP, where the small nanoparticles are all present inside the pore structures.

Electrochemical performances of Co$_3$O$_4$–COP composites

Lithium-ion batteries (LIBs) are important power sources not only for popular electronic devices but also for future energy storage systems, such as an electrical vehicle and a grid system.[32] In order to develop the high-performance of LIBs that satisfy the requirements for future energy storage systems, a great number of efforts have been made such as carbon-based nanomaterials,[33] transition metal oxides,[34,35] and the intercalation based materials.[36] Among these, metal oxides attracted great attention due to their higher theoretical specific capacity (~900 mA h g^{-1}) compared to current commercialized carbon-based materials (~300 mA h g^{-1}).[37] However, there exists a drawback to use metal oxide electrodes owing to a poor cycle life resulted from large volume change and concomitant particle agglomeration that is caused by continuous insertion and extraction of lithium ions. The pulverization of the electrode occurs by the significant volume change, further provoking the failures in the electrical contact between the electrode and current collector. The affiliated agglomeration of the nanoparticles is also highly obstructive to electrolyte penetration.[38] These side effects ultimately lead to huge reduction of cyclic performance. In order to improve the cyclability of metal oxide-based electrodes, therefore, several synthetic strategies have been demonstrated such as the fabrication of multi-layered structures,[39] and the application of porous substrates which can offer rooms to accommodate the volume expansion of electrodes, and prevent a rapid agglomeration of nanoparticles.[40,41] However, these synthetic approaches always accompany sophisticated, costly manipulations, which hinder the possibility of commercialization. We introduced Co$_3$O$_4$ nanocomposites incorporated into COPs, which can be prepared *via* a facile synthesis, and the composites present improved cyclic performance as an anode for LIBs.

The electrochemical performance of npCOP and nwCOP was investigated by galvanostatic charge/discharge cycling at different current densities using 2032 coin-type half cells. The working electrode was prepared by mortar slurry mixing and metallic lithium foil was used as counter/reference electrodes. All of the C-rates in this study were based on 1C (890 mA g^{-1}), and all of the current densities and specific capacities were based on the mass of the active material only, not the composite. Fig. S5† displays the charge/discharge profiles of the

This journal is © The Royal Society of Chemistry 2015

J. Mater. Chem. A, 2015, **3**, 15489–15497 | **15493**

npCOP and nwCOP in their first and second cycles with a current density of 0.06C (50 mA g^{-1}). In the first discharge step, both composites present a long voltage plateau at 1.09 V, followed by a sloping curve down to the cutoff voltage of 0.05 V. During the first charge (delithiation) step, both samples showed plateau around 1.7 V and delivered a specific capacity of 959 and 886 mA h g^{-1} for npCOP and nwCOP, respectively. This voltage profile corresponds to a typical characteristic Co$_3$O$_4$ conversion reaction: Co$_3$O$_4$ + 8Li$^+$ + 8e$^-$ ↔ 3Co + 4Li$_2$O.[42] Cyclic voltammograms of npCOP and nwCOP also proved the conversion reaction with reversible reduction and oxidation peaks (Fig. S6c and d†). Both composites showed low Coulombic efficiency in the first cycle (52% for npCOP and 66% for nwCOP) due to the formation of a solid electrolyte interphase (SEI) layer during the discharge process[37] as well as inevitable Li ion trapping.[43] From the second cycle, both composites exhibited reversible charge/discharge cycles with a capacity of 967 mA h g^{-1} for npCOP, and 898 mA h g^{-1} for nwCOP. On the other hand, COP treated at 300 °C only shows modest capacity up to 50 mA h g^{-1} at a current density of 0.06C (50 mA g^{-1}) (Fig. S6b†) with insignificant reaction in the CV curve (Fig. S6a†).

The rate capability of the composites was measured at different current densities of 0.06C (50 mA g^{-1}), 0.24C (200 mA g^{-1}), 0.96C (1000 mA g^{-1}), and 1.92C (2000 mA g^{-1}) (Fig. 4). As the current density increased from 0.06C to 1.92C, the capacity of npCOP decreased from 1237 to 580 mA h g^{-1}, indicating 47% capacity retention. In the case of nwCOP, the capacity decreased from 1109 to 835 mA h g^{-1}, indicating 75% capacity retention. This matches well with cyclic rate performance, showing 47% and 69.2% of capacity retention from 0.06C to 1.96C, for npCOP and nwCOP, respectively (Fig. S7†). However, interestingly, the cyclic performance between npCOP and nwCOP was variant from the rate capability of the composite. Fig. 5 shows capacity–cycle curves of npCOP and nwCOP at current densities of 0.96C (1000 mA g^{-1}) and 1.92C (2000 mA g^{-1}). After the 60th cycle, nwCOP showed a capacity of 601 mA h g^{-1} at a current density of 0.96C (1000 mA g^{-1}) and 434 mA h g^{-1} at 1.92C (2000 mA g^{-1}). On the other hand, the npCOP showed 978 mA h g^{-1} of capacity at a current density of 0.96C (1000 mA g^{-1}), and 457 mA h g^{-1} at a density of 1.92C (2000 mA g^{-1}) after the 60th cycle. Thus, the capacity of nwCOP, despite good rate capability at high current density, rapidly drops by about 25% (Fig. 5b), however, npCOP shows 35% increase of capacity even after the 60th cycle at a rate of 0.96C (1000 mA g^{-1}) (Fig. 5a). Different behaviors in rate capability and cyclic performance between npCOP and nwCOP can be ascribed to different porosities and locations of the Co$_3$O$_4$ nanoparticles in the COP structure (Fig. 5 inset). Since the nanowires in nwCOP are mostly located in the larger pores of the polymer structure, which gives a higher total pore volume of the structure, nwCOP could show good rate capability due to its large pore distribution and close proximity for rapid Li$^+$ transport. However, when the nanowires undergo volume expansion/shrinkage repeatedly over cycling, they lose the contact with COP and consequently agglomerate, thus behaving like bulk counterparts and decaying the capacity. For the npCOP, on the contrary, the nanoparticles are deeply incorporated into the COP structure, which results in lower pore

volume and narrow pore distribution, therefore, npCOP exhibits low capacity at high current density due to slow Li$^+$ penetration. As Li$^+$ ions are inserted deep inside of npCOP via a continuous charge/discharge process, the nanoparticles are fully reacted with Li$^+$ ions and npCOP exhibits great cyclic performance with the capacity up to ~980 mA h g^{-1}. The extra capacity of npCOP over the theoretical capacity (~900 mA h g^{-1}) is attributed to the reversible formation/decomposition of polymers with the catalytic effect of Co$_3$O$_4$ nanoparticles, which can be also found in transition metal–polymer composites (C/Sn[44] and CoO[45]).

A good cyclic stability of npCOP is also supported with TEM and XRD measurements. After the 60th cycle, the active materials were collected and analyzed by TEM and XRD. The TEM image confirms that the nanoparticles in npCOP retained their original morphology, however, the nanowires were mostly decomposed because of volume change and subsequent agglomeration (Fig. S8†). The XRD patterns of the composites show that Li$_x$Co$_3$O$_4$ intermediates were formed after the 60th cycle with a strong intensity of Co$_3$O$_4$, Li$_2$O, and Li$_x$Co$_3$O$_4$ (Fig. S9†). The formation of Li$_x$Co$_3$O$_4$ intermediates may result from fast discharge rates.[46] The intensity of npCOP is much stronger than that of nwCOP even measured under the same conditions, indicating that nanowires in nwCOP become amorphous owing to collapse of the crystal structure.

Of importance is that bare Co$_3$O$_4$ nanoparticles show poor cyclability with the capacity less than 200 mA h g^{-1} after the 20th cycle.[47] Comparing with the capacities reported from the literature (Table S3†), the capacity with npCOP after the 60th cycle is highly comparable, in terms of cyclic stability with a rapid
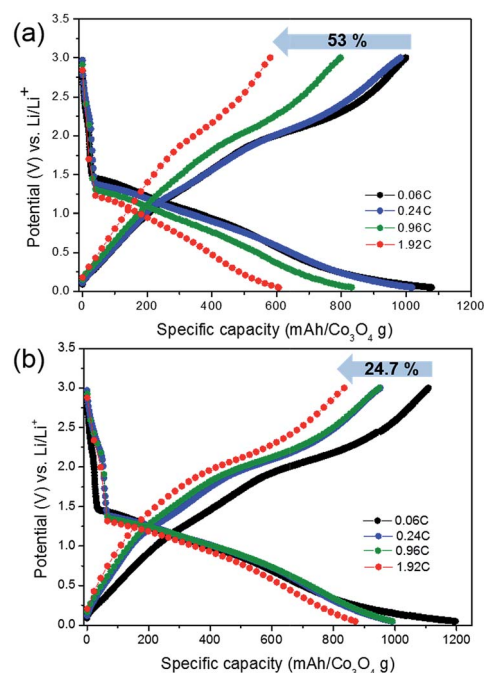

Fig. 4 Galvanostatic voltage profiles of (a) npCOP and (b) nwCOP at different current rates. The voltage profile is illustrated after the 10th cycle, and the capacity change from 0.06C to 1.92C is shown in percentage values.

15494 | J. Mater. Chem. A, 2015, **3**, 15489–15497

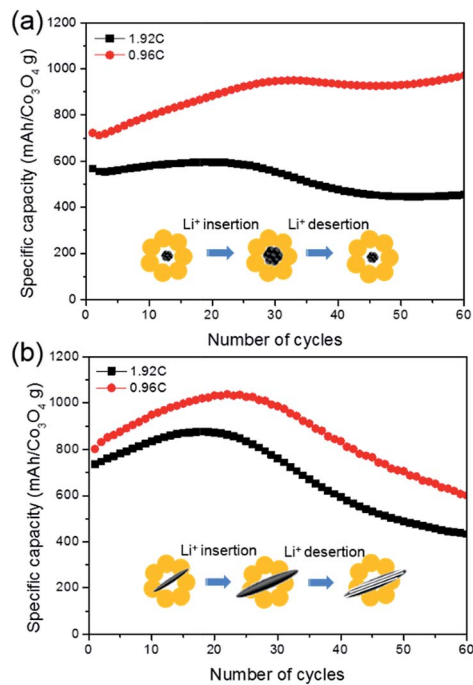This journal is © The Royal Society of Chemistry 2015

Fig. 5 Cyclic performance of (a) npCOP and (b) nwCOP. Inset displays a plausible mechanism that improves the cyclic stability of the nanocomposites induced by location of nanoparticles.

charge and discharge.[14,37,48,49] A soft template of COP has prevented a rapid volume expansion and agglomeration of nanoparticles, providing a new method for improving the efficiency of metal oxide based LIBs.

Catalytic activities of Co_3O_4–COP composites

Co_3O_4 nanoparticles are also known as a good catalyst for CO oxidation. In order to demonstrate the superior stability of caged nanoparticles, we investigated CO oxidation efficiencies and cycle life. The reactivity of CO oxidation on the Co_3O_4 surface mainly depends on the amount of the exposed Co^{3+} cations on the surface, since the Co^{3+} ion of Co_3O_4 at octahedral site is the active site for CO oxidation, and Co^{2+} ion at tetrahedral site is almost inactive.[50] Fig. 6a shows chronographic CO oxidation reactivity on npCOP and nwCOP. The first two cycles of CO conversion exhibit the temperature at which 100% CO conversion is observed, T_{100} was 100 °C for npCOP, and 110 °C for nwCOP. These values are comparable or better than various Co_3O_4 nanoparticles and their composites, such as Co_3O_4 in SiO_2 nanocapsules ($T_{100} = 150$ °C),[51] Co_3O_4 in ZIF-8 frameworks (150 °C),[52] Co_3O_4 templated by KIT-6 (100 °C),[53] Co_3O_4 nanoparticles with pre-heat treatment (130 °C),[54] Co_3O_4 microdiscs (100 °C),[55] Co_3O_4 nanobelts and nanocubes (80 °C)[56] (Table S4†). The good catalytic activity of npCOP and nwCOP is attributed to main crystal planes exposed on the surface, which corresponds to XPS observation (Fig. S3b†). The npCOP shows reversible catalytic activity with no change of conversion efficiency between the 1st and 2nd cycle, while the nwCOP displays a jump in the range between 90 and 100 °C in the 2nd cycle. We assume that the ignition of CO caused the conversion jump near at

90 °C. The overall conversion efficiency of npCOP is higher than that of nwCOP, attributing to quantitatively larger amounts of nanoparticles in the structure with a concomitant high surface area. The thermogravimetric analyses show that COP, npCOP, and nwCOP are thermally stable up 300 °C in an oxidative environment and up to 400 °C in an inert atmosphere (Fig. S10†). The oxidative degradation of COPs under atmospheric conditions results in lower thermal stability in air. The thermal stability of the composites facilitates a long-term catalytic reaction at high temperature.

When the samples are tested for long-term stability, nwCOP exhibits higher stability than npCOP (Fig. 6b). Both the composites show initially 8% of CO conversion at 80 °C, and conversion efficiency increased up to 11% for nwCOP while the efficiency decreased to 6% for npCOP after 37 h. We believe that the nanowires in nwCOP have more active sites of Co^{3+} than npCOP, because they are mostly exposed at the larger pores of the COP structure, therefore they could finally result in good cyclic stability. The IR spectrum can be correlated to elucidate this assumption. The peak at 560 cm^{-1}, which is from Co^{3+} and oxygen vibration, is stronger for nwCOP than npCOP (Fig. S4†). The DRIFT spectra measured after CO exposure for 37 h also support the idea (Fig. S11†). The spectra display two distinct peaks at 2220 and 2340 cm^{-1}, indicating the presence of CO and CO_2 molecules, respectively.[57] The relative intensity of nwCOP is stronger than that of npCOP, resulting from close proximity and the favorable interaction between CO gas molecules and the Co_3O_4 surface. We note, however, that our findings need to be further investigated with respect to the quantitative amount of surficial planes and active sites in both the composites.
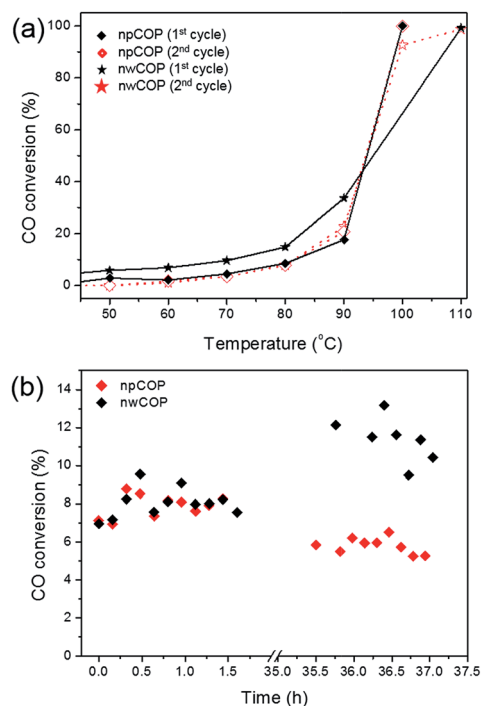

Fig. 6 (a) CO conversion on npCOP and nwCOP catalysts, and (b) long-term stability test result of npCOP and nwCOP measured at 80 °C for 37 h.

Conclusions

A facile strategy to generate highly uniform Co_3O_4 nanostructures within covalent organic polymers (COPs) has been introduced in this study. Fine nanoparticles with different morphologies are obtained *via* a caging template effect of COPs with amide functionalities, and the morphology of nanoparticles can be adjusted by simply varying the solvents. Since the morphology of particles is mainly governed by the pore shape of COPs, production of nanoparticles with this synthetic approach could provide a new way to look into the inner structure of amorphous porous polymer networks. The composites with nanoparticles and nanowires are purely crystalline and highly porous, which provides many potential applications. The electrochemical performance of the composites demonstrated superior capacity and cyclic stability at a high current density ($\sim$980 mA h g^{-1} at the 60th cycle at a current density of 1000 mA g^{-1}). In a catalytic reaction with carbon monoxide, the composites exhibit a remarkable stability and catalytic performance ($T_{100} = 100$ °C). The simple synthetic process along with superior performance for energy storage and conversion applications clearly offers stimulating future opportunities to generate a variety of oxide nanostructures within porous polymers.

Acknowledgements

References

1 C. Burda, X. B. Chen, R. Narayanan and M. A. El-Sayed, *Chem. Rev.*, 2005, **105**, 1025–1102.

2 N. Tetreault and M. Gratzel, *Energy Environ. Sci.*, 2012, **5**, 8506–8516.

3 B. Z. Tian, X. L. Zheng, T. J. Kempa, Y. Fang, N. F. Yu, G. H. Yu, J. L. Huang and C. M. Lieber, *Nature*, 2007, **449**, 885–888.

4 D. Astruc, F. Lu and J. R. Aranzaes, *Angew. Chem., Int. Ed.*, 2005, **44**, 7852–7872.

5 G. A. Somorjai and J. Y. Park, *Top. Catal.*, 2008, **49**, 126–135.

6 C. Peng, B. Jiang, Q. Liu, Z. Guo, Z. Xu, Q. Huang, H. Xu, R. Tai and C. Fan, *Energy Environ. Sci.*, 2011, **4**, 2035–2040.

7 C. T. Yavuz, J. T. Mayo, W. W. Yu, A. Prakash, J. C. Falkner, S. Yean, L. L. Cong, H. J. Shipley, A. Kan, M. Tomson, D. Natelson and V. L. Colvin, *Science*, 2006, **314**, 964–967.

8 P. Poizot, S. Laruelle, S. Grugeon, L. Dupont and J. M. Tarascon, *Nature*, 2000, **407**, 496–499.

9 X. H. Guo, W. W. Xu, S. R. Li, Y. P. Liu, M. L. Li, X. N. Qu, C. C. Mao, X. J. Cui and C. H. Chen, *Nanotechnology*, 2012, **23**, 465401.

10 S. H. Sun, C. B. Murray, D. Weller, L. Folks and A. Moser, *Science*, 2000, **287**, 1989–1992.

11 S. Goel, Z. Wu, S. I. Zones and E. Iglesia, *J. Am. Chem. Soc.*, 2012, **134**, 17688–17695.

12 Z. Guo, C. Xiao, R. V. Maligal-Ganesh, L. Zhou, T. W. Goh, X. Li, D. Tesfagaber, A. Thiel and W. Huang, *ACS Catal.*, 2014, **4**, 1340–1348.

13 G. Lu, S. Li, Z. Guo, O. K. Farha, B. G. Hauser, X. Qi, Y. Wang, X. Wang, S. Han, X. Liu, J. S. DuChene, H. Zhang, Q. Zhang, X. Chen, J. Ma, S. C. J. Loo, W. D. Wei, Y. Yang, J. T. Hupp and F. Huo, *Nat. Chem.*, 2012, **4**, 310–316.

14 K. M. Shaju, F. Jiao, A. Debart and P. G. Bruce, *Phys. Chem. Chem. Phys.*, 2007, **9**, 1837–1842.

15 G. X. Wang, H. Liu, J. Horvat, B. Wang, S. Z. Qiao, J. Park and H. Ahn, *Chem.–Eur. J.*, 2010, **16**, 11020–11027.

16 G. J. D. Soler-illia, C. Sanchez, B. Lebeau and J. Patarin, *Chem. Rev.*, 2002, **102**, 4093–4138.

17 D. Y. Zhao, Q. S. Huo, J. L. Feng, B. F. Chmelka and G. D. Stucky, *J. Am. Chem. Soc.*, 1998, **120**, 6024–6036.

18 A. P. Cote, A. I. Benin, N. W. Ockwig, M. O'Keeffe, A. J. Matzger and O. M. Yaghi, *Science*, 2005, **310**, 1166–1170.

19 R. Dawson, A. I. Cooper and D. J. Adams, *Prog. Polym. Sci.*, 2012, **37**, 530–563.

20 H. A. Patel, J. Byun and C. T. Yavuz, *J. Nanopart. Res.*, 2012, **14**, 881.

21 H. A. Patel, S. H. Je, J. Park, D. P. Chen, Y. Jung, C. T. Yavuz and A. Coskun, *Nat. Commun.*, 2013, **4**, 1357.

22 M. X. Tan, Y. N. Sum, J. Y. Ying and Y. G. Zhang, *Energy Environ. Sci.*, 2013, **6**, 3254–3259.

23 A. Thomas, *Angew. Chem., Int. Ed.*, 2010, **49**, 8328–8344.

24 S. Wan, F. Gándara, A. Asano, H. Furukawa, A. Saeki, S. K. Dey, L. Liao, M. W. Ambrogio, Y. Y. Botros, X. Duan, S. Seki, J. F. Stoddart and O. M. Yaghi, *Chem. Mater.*, 2011, **23**, 4094–4097.

25 W. G. Lu, W. M. Verdegaal, J. M. Yu, P. B. Balbuena, H. K. Jeong and H. C. Zhou, *Energy Environ. Sci.*, 2013, **6**, 3559–3564.

26 Y. L. Zhang, S. Wei, F. J. Liu, Y. C. Du, S. Liu, Y. Y. Ji, T. Yokoi, T. Tatsumi and F. S. Xiao, *Nano Today*, 2009, **4**, 135–142.

27 Y. Zhou, Z. H. Xiang, D. P. Cao and C. J. Liu, *Chem. Commun.*, 2013, **49**, 5633–5635.

28 S. H. Kim, C. H. Jung, N. Sahu, D. Park, J. Y. Yun, H. Ha and J. Y. Park, *Appl. Catal., A*, 2013, **454**, 53–58.

29 T.-T.-T. Nguyen, F.-X. Simon, N. S. Khelfallah, M. Schmutz and P. J. Mesini, *J. Mater. Chem.*, 2010, **20**, 3831–3833.

30 S. C. Petitto and M. A. Langell, *J. Vac. Sci. Technol., A*, 2004, **22**, 1690–1696.

31 Q. Jiang and M. D. Ward, *Chem. Soc. Rev.*, 2014, **43**, 2066–2079.

32 P. G. Bruce, B. Scrosati and J. M. Tarascon, *Angew. Chem., Int. Ed.*, 2008, **47**, 2930–2946.

15496 | *J. Mater. Chem. A*, 2015, **3**, 15489–15497

This journal is © The Royal Society of Chemistry 2015

33 N. A. Kaskhedikar and J. Maier, *Adv. Mater.*, 2009, **21**, 2664–2680.

34 Y. S. Hu, L. Kienle, Y. G. Guo and J. Maier, *Adv. Mater.*, 2006, **18**, 1421–1426.

35 P. Meduri, C. Pendyala, V. Kumar, G. U. Sumanasekera and M. K. Sunkara, *Nano Lett.*, 2009, **9**, 612–616.

36 C. Q. Feng, J. Ma, H. Li, R. Zeng, Z. P. Guo and H. K. Liu, *Mater. Res. Bull.*, 2009, **44**, 1811–1815.

37 Z. S. Wu, W. C. Ren, L. Wen, L. B. Gao, J. P. Zhao, Z. P. Chen, G. M. Zhou, F. Li and H. M. Cheng, *ACS Nano*, 2010, **4**, 3187–3194.

38 X. Wang, H. Guan, S. M. Chen, H. Q. Li, T. Y. Zhai, D. M. Tang, Y. Bando and D. Golberg, *Chem. Commun.*, 2011, **47**, 12280–12282.

39 W. L. Yao, J. Yang, J. L. Wang and Y. Nuli, *J. Electrochem. Soc.*, 2008, **155**, A903–A908.

40 F. Li, Q. Q. Zou and Y. Y. Xia, *J. Power Sources*, 2008, **177**, 546–552.

41 H. J. Liu, S. H. Bo, W. J. Cui, F. Li, C. X. Wang and Y. Y. Xia, *Electrochim. Acta*, 2008, **53**, 6497–6503.

42 W. Y. Li, L. N. Xu and J. Chen, *Adv. Funct. Mater.*, 2005, **15**, 851–857.

43 J. Chen, *Materials*, 2013, **6**, 156–183.

44 Y. H. Xu, J. C. Guo and C. S. Wang, *J. Mater. Chem.*, 2012, **22**, 9562–9567.

45 S. Grugeon, S. Laruelle, L. Dupont and J. M. Tarascon, *Solid State Sci.*, 2003, **5**, 895–904.

46 D. Larcher, G. Sudant, J. B. Leriche, Y. Chabre and J. M. Tarascon, *J. Electrochem. Soc.*, 2002, **149**, A234–A241.

47 G. X. Wang, Y. Chen, K. Konstantinov, M. Lindsay, H. K. Liu and S. X. Dou, *J. Power Sources*, 2002, **109**, 142–147.

48 N. Du, H. Zhang, B. Chen, J. B. Wu, X. Y. Ma, Z. H. Liu, Y. Q. Zhang, D. Yang, X. H. Huang and J. P. Tu, *Adv. Mater.*, 2007, **19**, 4505–4509.

49 X. Wang, X. L. Wu, Y. G. Guo, Y. T. Zhong, X. Q. Cao, Y. Ma and J. N. Yao, *Adv. Funct. Mater.*, 2010, **20**, 1680–1686.

50 X. W. Xie, Y. Li, Z. Q. Liu, M. Haruta and W. J. Shen, *Nature*, 2009, **458**, 746–749.

51 N. Yan, Q. Chen, F. Wang, Y. Wang, H. Zhong and L. Hu, *J. Mater. Chem. A*, 2013, **1**, 637–643.

52 W. X. Wang, Y. W. Li, R. J. Zhang, D. H. He, H. L. Liu and S. J. Liao, *Catal. Commun.*, 2011, **12**, 875–879.

53 S. J. Sun, Q. M. Gao, H. L. Wang, J. K. Zhu and H. L. Guo, *Appl. Catal., B*, 2010, **97**, 284–291.

54 H. K. Lin, H. C. Chiu, H. C. Tsai, S. H. Chien and C. B. Wang, *Catal. Lett.*, 2003, **88**, 169–174.

55 H. W. Che, A. F. Liu, Q. R. Fu and R. J. Jiang, *Mater. Lett.*, 2013, **93**, 240–242.

56 L. H. Hu, K. Q. Sun, Q. Peng, B. Q. Xu and Y. D. Li, *Nano Res.*, 2010, **3**, 363–368.

57 F. Grillo, M. M. Natile and A. Glisenti, *Appl. Catal., B*, 2004, **48**, 267–274.

This journal is © The Royal Society of Chemistry 2015

J. Mater. Chem. A, 2015, **3**, 15489–15497 | **15497**